

# SLAM&Render: A Benchmark for the Intersection Between Neural Rendering, Gaussian Splatting and SLAM

<https://samuel-cerezo.github.io/SLAM&Render>

Samuel Cerezo<sup>1</sup>, Gaetano Meli<sup>1,2</sup>, Tomás Berriel Martins<sup>1</sup>, Kirill Safronov<sup>2</sup> and Javier Civera<sup>1</sup>

**Abstract**—Models and methods originally developed for novel view synthesis and scene rendering, such as Neural Radiance Fields (NeRF) and Gaussian Splatting, are increasingly being adopted as representations in Simultaneous Localization and Mapping (SLAM). However, existing datasets fail to include the specific challenges of both fields, such as multi-modality and sequentiality in SLAM or generalization across viewpoints and illumination conditions in neural rendering. To bridge this gap, we introduce **SLAM&Render**, a novel dataset designed to benchmark methods in the intersection between SLAM and novel view rendering. It consists of 40 sequences with synchronized RGB, depth, IMU, robot kinematic data, and ground-truth pose streams. By releasing robot kinematic data, the dataset also enables the assessment of novel SLAM strategies when applied to robot manipulators. The dataset sequences span five different setups featuring consumer and industrial objects under four different lighting conditions, with separate training and test trajectories per scene, as well as object rearrangements. Our experimental results, obtained with several baselines from the literature, validate **SLAM&Render** as a relevant benchmark for this emerging research area.

## I. INTRODUCTION

Simultaneous Localization and Mapping, typically known by its acronym SLAM, is a key enabler for autonomous robot navigation and understanding. The goal is to simultaneously estimate the robot’s pose while creating a globally consistent representation or map of its surroundings, using only the data from the robot’s onboard sensors. After decades of intense research, several highly performing methods for geometric SLAM in rigid environments are available [1]. However, many research challenges remain [2]. SLAM differs from alternative approaches to 3D reconstruction (e.g., Structure from Motion [3]) by its online, real-time and multi-modal features, making it well-suited for robotic applications and requirements.

Novel view synthesis, seemingly distant from robot SLAM, has experienced a resurgence due to groundbreaking research in neural radiance fields, also known as NeRFs [4]. Nevertheless, it has been quickly adopted as a map representation in visual [5], [6] and LiDAR [7] SLAM pipelines. On the other hand, Gaussian Splatting [8], developed as a much faster alternative to NeRFs, has had an even bigger impact

<sup>1</sup>Authors are with the Departamento de Informática e Ingeniería de Sistemas, Universidad de Zaragoza, 50018 Zaragoza, ES. E-mails: {samueladriancerezo, tberriel, jcivera}@unizar.es

<sup>2</sup>Authors are with the Technology & Innovation Center, KUKA Deutschland GmbH, 86165 Augsburg, DE. E-mails: {gaetano.meli, kirill.safronov}@kuka.com

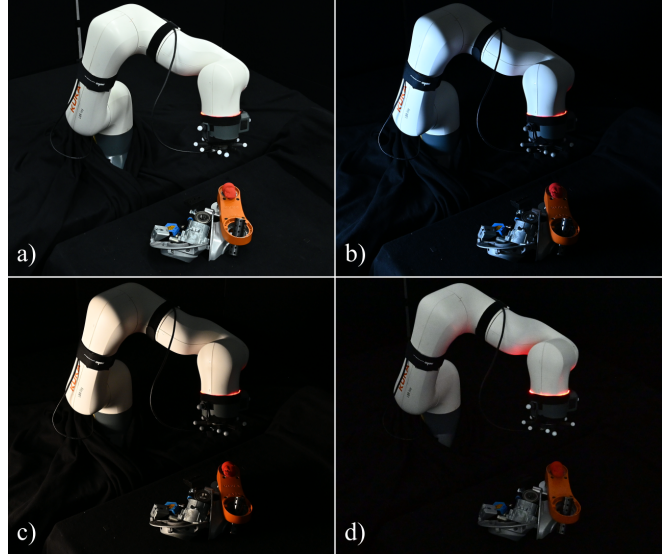


Fig. 1. Illustration of the capture setup for our **SLAM&Render** dataset, recorded from a Intel RealSense at the end effector of a robotic arm that moves around a set of objects on a table. See the four different light conditions present in our dataset: a) natural, b) cold, c) warm, and d) dark

in visual SLAM [9], [10], [11], [12]. Refer to the recent survey by Tosi et al. [13] for a comprehensive overview of references and in-depth discussions on how these two paradigms are influencing the field of SLAM.

Our work is motivated by this emerging trend intersecting visual SLAM, neural rendering and Gaussian splatting. Specifically, we argue that there is a lack of public datasets and benchmarks that explicitly address this area of research. Therefore, we introduce **SLAM&Render**, a novel dataset for benchmarking methods at the intersection of the aforementioned fields. It includes 40 sequences with synchronized RGB, depth, IMU, robot kinematic data, intrinsic and extrinsic camera parameters and ground-truth data. The sequences cover five setups with consumer and industrial objects captured under varying lighting conditions and include separate training/test trajectories and object rearrangements.

All data is available online under the Creative Commons Attribution license (CC-BY 4.0) at the website. Additional information, example code and videos for visual inspection of the dataset is also included.

Year	Dataset	Use	RGB	Depth	IMU	Enc.	GT	Ill.	Rearr.	TS.
2014	DTU [14]	NVS	✓	✓	✗	✗	✓	✓	✗	✗
2014	JIGSAWS [15]	Motion Model.	✓	✗	✗	✓	✗	✗	✗	✗
2015	YCB object and Model set [16]	Robotic Manip.	✗	✗	✗	✓	✓	✗	✗	✗
2016	EuRoC [17]	SLAM	✓	✗	✓	✗	✓	✓	✗	✓
2017	Tanks and Temples [18]	NVS	✓	✓	✗	✗	✗	✗	✗	✗
2018	TUM VI [19]	Odom.	✓	✗	✓	✗	(✓)	✗	✗	✗
2019	OpenLORIS-Scene [20]	SLAM	✓	✓	✓	✓	✗	✗	✗	✓
2019	Replica [21]	SLAM & NVS	✓	✓	✓	✗	✓	✗	✗	✓
2021	Mip-NeRF360 [22]	NVS	✓	✗	✗	✗	✗	✗	✗	✗
2023	ScanNet++ [23]	SLAM & NVS	✓	✓	✗	✗	✓	✗	✗	✓
2025	<b>SLAM&amp;Render</b>	SLAM & NVS	✓	✓	✓	✓	✓	✓	✓	✓

TABLE I

OVERVIEW OF COMMONLY USED DATASETS FOR SLAM AND NVS, INCLUDING AVAILABLE SENSOR MODALITIES (RGB, DEPTH, IMU, ENCODERS), GROUND TRUTH CAMERA POSE (GT), ILLUMINATION VARIATIONS (ILL.), SCENE REARRANGEMENTS (REARR.), AND TIME SYNCHRONIZATION (TS).

## II. RELATED WORK

Publicly available datasets have played a crucial role in advancing research in SLAM and Novel View Synthesis (NVS). In Table I, we provide an overview of the most relevant datasets that are instrumental to these fields of study.

### A. Datasets for SLAM

The EuRoC dataset [17] provides visual-inertial data from a Micro Aerial Vehicle, comprising two batches: one collected in an industrial environment for evaluating visual SLAM algorithms, and the other in a room for 3D environment reconstruction. Several challenges such as varying image brightness and dynamic scenes, are included. The TUM VI dataset [19] is designed for evaluating odometry algorithms. It includes RGB images, photometric calibration, and synchronized IMU data. Ground-truth poses at the start and end of the sequences are provided. The dataset also includes evaluations of state-of-the-art methods. Depth images are not present in this collection. OpenLORIS-Scene dataset [20] consists of visual-inertial and odometry data to benchmark SLAM and scene understanding algorithms in everyday scenarios. For data collection a wheeled robot equipped with a Realsense D435i camera, encoders and a LiDAR sensor was used. In the context of synthetic datasets, the Replica dataset [21] contains 18 photorealistic indoor reconstructions at room and building scales. It features dense 3D meshes, HDR textures, and reflective surfaces. However, neither changes in illumination or rearrangements of objects within the same scene are included.

### B. Datasets for Novel View Synthesis.

Despite the popularity of NeRFs, most datasets used for evaluation sample frames along a single camera trajectory, often lacking the diversity and complexity of real-world settings. DTU [14] was introduced for evaluating multi-view stereo techniques using a robotic setup with a structured light scanner. It contains a wide variety of scenes with different object types and lighting conditions. Tanks and Temples [18] was developed for image-based 3D reconstruction. It was captured in realistic, non-laboratory settings using an industrial laser scanner for ground-truth. It includes both

indoor and outdoor scenes. Recently, Mip-NeRF360 [22] introduced a dataset for high-quality novel view synthesis. It captured camera trajectories around a central object in indoor and outdoor scenarios with detailed backgrounds. Then, ScanNet++ [23] was introduced to benchmark 3D scene understanding methods. It combines 3D laser scans, DSLR images, and RGB-D sequences. It includes semantic annotations for diverse and ambiguous scenarios and is the first to use independent camera trajectories for NVS evaluation. However, it does not contain IMU, kinematic data or controlled illumination changes.

In the context of datasets containing kinematic data, the YCB Object and Model Set [16] provides object manipulation data with joint poses but does not include visual data. On the other hand, the JIGSAWS dataset [15] includes kinematic data from the da Vinci surgical robot and stereoscopic images of surgical tasks, providing a rich data source to study human-robot interaction. However, the dataset purpose makes it very domain-specific.

Unlike the existing datasets, the one presented in this work offers a comprehensive and diverse set of sequences designed to benchmark methods in the intersection between SLAM and novel view rendering. The dataset includes 40 sequences with synchronized streams of RGB images, depth, IMU, robot kinematic data, and ground-truth poses. The sequences cover five distinct setups with both consumer and industrial objects, captured under four lighting conditions. Each scene includes separate trajectories for training and testing, and variations in object arrangement to evaluate generalization. To the best of our knowledge, this is the first dataset containing multi-sensor and kinematic data collected in sequences characterized by varying lighting conditions, object rearrangements, occlusions, and time-synchronization (see Table I).

## III. NOTATION

### A. Convention for rigid transformations

Rigid transformations from a reference frame  $A$  to another reference frame  $B$  are defined as

$$\mathbf{T}_A^B = \begin{bmatrix} \mathbf{R}_A^B & \mathbf{p}_A^B \\ \mathbf{0}_{1 \times 3} & 1 \end{bmatrix} \in SE(3),$$

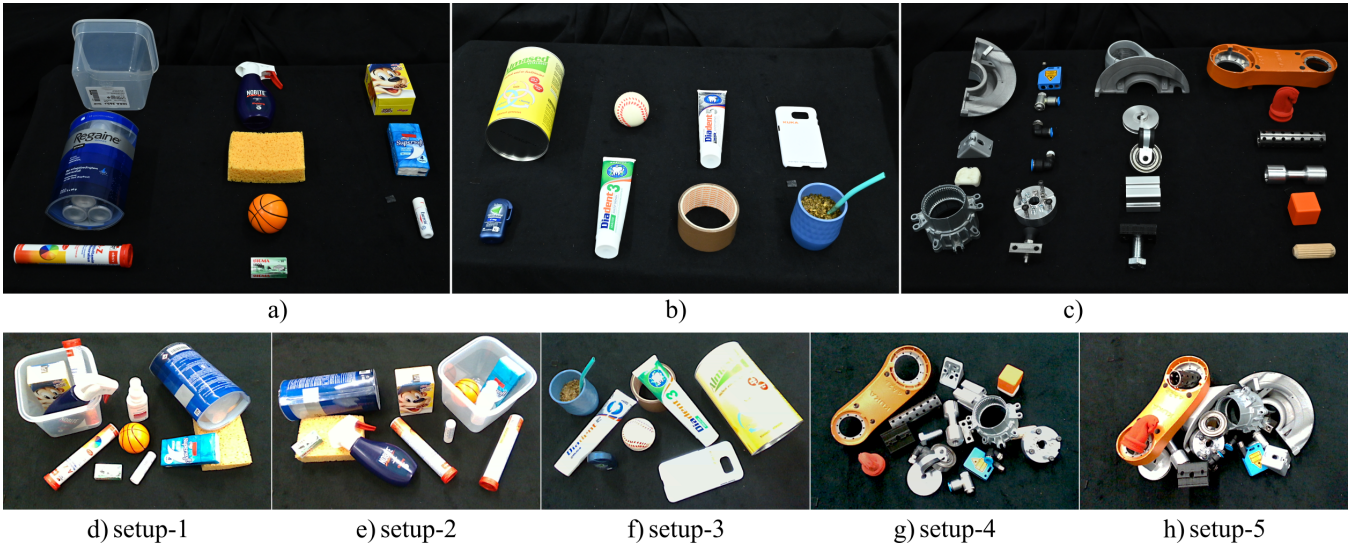


Fig. 2. Illustration of the objects included in **SLAM&Render**: a-b) supermarket goods, c) industrial goods, d)–h) object arrangements of the five setups.

where  $\mathbf{R}_A^B \in SO(3)$  and  $\mathbf{p}_A^B \in \mathbb{R}^3$  describe the orientation and the position of the frame  $A$  with respect to the reference frame  $B$ , respectively. Such rigid transformation will transform a 3D point  $\mathbf{p}^A \in \mathbb{R}^3$  ( $\tilde{\mathbf{p}}^A$  in homogeneous coordinates) to the reference frame  $B$  as  $\tilde{\mathbf{p}}^B = \mathbf{T}_A^B \tilde{\mathbf{p}}^A$

### B. Forward kinematics

A manipulator consists of a sequence of rigid bodies (*links*) connected through kinematic *joints*. Let  $\mathbf{x}(t) \in \mathbb{R}^m$  be the task variable to be controlled (e.g., end-effector pose) and  $\mathbf{q}(t) \in \mathbb{R}^n$  the vector of the variables describing the configuration (i.e., joint positions) of a given  $n$ -DOFs robot, with  $n \geq m$ . The relation between  $\mathbf{q}$  and  $\mathbf{x}$  is given by the forward kinematics equation

$$\mathbf{x}(t) = \mathbf{f}(\mathbf{q}(t)), \quad (1)$$

where  $\mathbf{f}(\cdot)$  is, in general, a nonlinear function allowing for the computation of the task variables starting from the robot configuration.

## IV. THE **SLAM&RENDER** DATASET

The proposed dataset comprises 40 sequences that include both inertial and RGB-D data. These were recorded using an Intel RealSense D435i camera, mounted in an eye-to-hand configuration on a KUKA LBR iisy 3 R760 manipulator. Additionally, kinematic data were collected from the manipulator. In particular, the dataset contains the robot configurations  $\mathbf{q}(t)$  along the motion and the corresponding flange poses computed using Eq. (1). An external Motion Capture System (MCS) was used to obtain the ground-truth camera poses. All sequences were recorded in an environment where the objects were placed on a black background, surrounded by black panels featuring pictures that display complex and colorful patterns (see Sec. IV-A). Moreover, the dataset contains *train* and *test* camera trajectories recorded under the following four different lighting conditions:

- *natural* – Natural light of the environment

- *cold* – Cold artificial light
- *warm* – Warm artificial light
- *dark* – No light.

This enables our dataset to be used with classical SLAM approaches [2] as well as newer Gaussian splatting- and NeRF-based paradigms [13], which are particularly sensitive to lighting conditions and may require proper training to perform effectively. Therefore, this dataset feature ensures that SLAM algorithms are tested and trained in environments that reflect real-world variability, ultimately evaluating their performance and reliability in practical applications. Although the KUKA LBR iisy 3 R760 manipulator has a repeatability parameter<sup>1</sup> of  $\pm 0.1$  mm, we release the joint configurations and flange poses for all the sequences belonging to train and test trajectories. As a result, the camera pose estimation conducted by any SLAM algorithm on this dataset remains unaffected by variations in joint configurations. Furthermore, with smooth robot motions, the camera performs loop closures in both train and test trajectories (see Fig. 3). The dataset sequences capture various scenes that include both opaque and transparent objects, as well as reflective and non-reflective items. Furthermore, the same object may be present in different positions and orientations across the sequences, creating arrangements with varying levels of occlusion. The dataset features the following five distinct scenes (see Fig. 2):

- *setup-1* and *setup-2* include a set of common supermarket goods including transparent objects
- *setup-3* includes a different set of common supermarket goods including only opaque objects
- *setup-4* contains industrial objects
- *setup-5* contains industrial objects in a cluttered arrangement.

We additionally release a collection of images capturing

<sup>1</sup>The repeatability parameter gives a measure of the manipulator’s ability to return to a previously reached position. The smaller the value, the higher the repeatability.

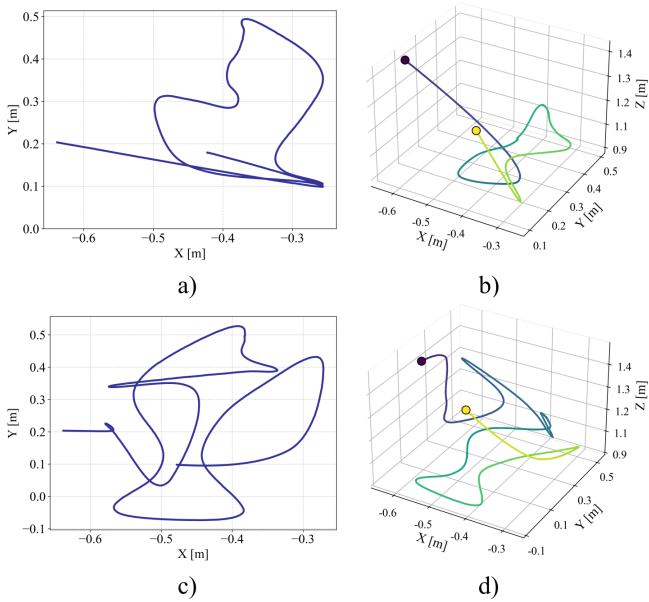


Fig. 3. Our **SLAM&Render** dataset contains train and test camera trajectories. From top left to bottom right: a) 2D representation of train trajectory, b) 3D representation of train trajectory, c) 2D representation of test trajectory, and d) 3D representation of test trajectory. Blue and yellow points represent start and end points of the trajectories, respectively.

a chessboard calibration pattern to calibrate the intrinsic and extrinsic parameters of the camera. The calibration procedure, together with the estimation of extrinsic and intrinsic parameters, is detailed in Sec. IV-E.

Our website offers a collection of tools for data association, retrieval from ROS2 bag files, alignment, and synchronization.

#### A. Data acquisition

All RGB-D data were recorded at the optimal depth resolution<sup>2</sup> (848×480) and full frame rate (30 Hz) of the Intel RealSense D435i camera. The IMU data were acquired at a rate of 210 Hz, capturing synchronized readings from the gyroscope and accelerometer. All the dataset sequences were collected through a system based on Ubuntu 22.04 and ROS2 Humble. We used the software library Intel RealSense SDK 2.0<sup>3</sup> and its ROS2 wrapper<sup>4</sup> to record the camera data. While the depth and color images are initially unaligned, as they are captured by two distinct sensors, we used the built-in feature of the Intel ROS2 wrapper to register the depth images to the color images. This is achieved by projecting the depth images to 3D and then back-projecting them into the color camera view. The joint angles of the robot manipulator were collected using ROS2 at a frequency of 25 Hz.

To record ground-truth data, we employed an OptiTrack Motion Capture System (MCS) composed of twelve PrimeX 13W cameras installed around the robot cell. These cameras track the position and orientation of passive markers at

<sup>2</sup><https://dev.intelrealsense.com/docs/tuning-depth-cameras-for-best-performance>

<sup>3</sup><https://www.intelrealsense.com/sdk-2/>

<sup>4</sup><https://dev.intelrealsense.com/docs/ros2-wrapper>

a frequency of 120 Hz. The markers are mounted on a circular structure between the camera and the robot flange (see Fig. 4). This structure was printed using an industrial-grade 3D printer, ensuring high accuracy while tracking the markers. Additionally, we have added two markers on the flange and one marker on the camera itself to enhance the asymmetry of the marker setup.

To minimize reflections from the surrounding environment, non-reflective black panels were installed around the perimeter of the robot cell. Pictures featuring complex and colorful patterns have been placed on the black panels not to oversimplify the novel view synthesis of NeRF-based algorithms. Further, the metal table supporting the robot manipulator was covered with a black cloth.

The cold and warm lighting setups were obtained thanks to a Neewer 660 (50W) PRO LED lamp.

#### B. Dataset structure

Inspired by [24], our dataset is organized into sequences, which share the same structure across all setups. For the sake of simplicity, consider the following *setup-1* structure:

```

setup-1
├── natural/
│   ├── ...
├── warm/
│   ├── ...
├── cold/
│   ├── ...
├── dark/
│   ├── ...
├── intrinsics.yaml
└── extrinsics.yaml

```

Each lighting condition has a *train* and *test* sequence, which are organized in the same manner. For example, the structure of the *train* sequence is reported below.

```

train
├── rgb/
│   ├── 1739371345.939813614.png
│   ├── 1739371346.193981361.png
│   └── ...
├── depth/
│   ├── 1739371345.939813614.png
│   ├── 1739371346.193981361.png
│   └── ...
├── robot_data/
│   ├── joint_positions.txt
│   └── flange_poses.txt
├── associations.txt
├── imu.txt
├── groundtruth_raw.csv
└── groundtruth.txt

```

These folders and files contain the following data:

- `rgb/`: folder containing the timestamped color images (PNG format, 3 channels, 8 bits per channel);
- `depth/`: folder containing the timestamped depth images (PNG format, 1 channel, 16 bits per channel,

distance scaled by a factor of 1000). The depth images are already aligned with the RGB sensor;

- `associations.txt`: file listing all the temporal associations between the RGB and depth images (format: `rgb.timestamp rgb_file depth.timestamp depth_file`);
- `imu.txt`: file containing timestamped accelerometer and gyroscope readings (format: `timestamp ax ay az gx gy gz`);
- `groundtruth.txt`: file containing the timestamped ground-truth of the camera poses w.r.t world reference frame, expressed as a sequence of quaternions and translation vectors (format: `timestamp qx qy qz qw tx ty tz`) (see Sec. IV-D);
- `groundtruth_raw.csv`: file provided by the MCS containing ground-truth raw data of flange marker ring trajectory;
- `extrinsics.yaml`: file containing the transformation matrices of the reference frames involved in the data collection process (see Sec. IV-C);
- `intrinsics.yaml`: file containing the intrinsic calibration parameters of the camera (see Sec. IV-E);
- `robot_data/flange_poses.txt`: file containing the timestamped poses of the robot flange. Each pose is expressed w.r.t. the robot base as a quaternion and translation vector (format: `timestamp qx qy qz qw tx ty tz`);
- `robot_data/joint_positions.txt`: file reporting the timestamped angles of each robot joint (format: `timestamp q1 q2 q3 q4 q5 q6`).

The accelerometer data are provided in  $m/s^2$ , the gyroscope data in  $rad/s$ , and the ground-truth and flange positions in  $mm$ . All sequences are also available as ROS2 bag files.

### C. Reference frames

The reference frames shown in Fig. 4 were used in the data collection process to align the data coming from the camera, the robot and the MCS. These reference frames are described below.

- `robot_flange`: defined at the center of the real robot flange;
- `flange_marker_ring`: used by the MCS to locate the robot flange;
- `rgb_sensor`: optical center of the RGB sensor;
- `imu`: describing the IMU sensor pose;
- `base_marker_ring`: used by the MCS to locate the robot base;
- `robot_base`: defined at the center of the real robot base.

### D. Motion Capture System (MCS)

**Calibration.** To collect ground-truth data, twelve Optitrack PrimeX 13W cameras were used. These cameras were carefully positioned to focus on the robot flange from various angles, minimizing occlusion caused by the robot’s movements. The cameras were calibrated using the Motive

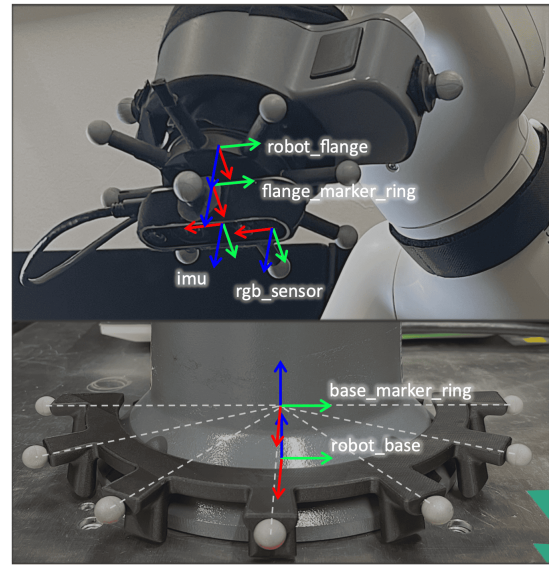


Fig. 4. Illustration of the reference frames involved in the data collection.

software<sup>5</sup> provided by Optitrack. This process involves waving a calibration wand, equipped with three passive markers, throughout the area to be captured. After the wanding process, Motive compares the 2D results from the individual cameras to reconstruct a 3D capture volume. The calibration process resulted in a mean 3D error of  $0.4\text{ mm}$ , indicating the level of convergence error between the twelve cameras.

**Synchronization.** The data from the MCS are initially unsynchronized. To ensure temporal alignment, for each sequence we retrieved the *capture starting time* provided by OptiTrack. Consequently, the ground-truth file we provide includes the corresponding Unix Epoch timestamp for each pose, calculated using the corresponding *capture starting time*. Following the approach presented in [25], the synchronization was validated by comparing the angular velocity estimated from the MCS with the gyroscope measurements from the IMU using cross-correlation (see Fig. 5). The

<sup>5</sup><https://optitrack.com/software/motive/>

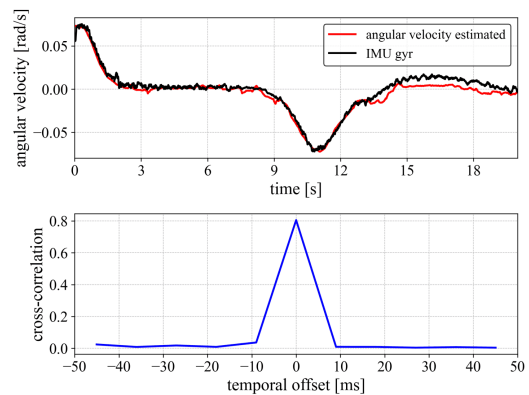


Fig. 5. Validation of time-synchronized data comparing the angular velocity estimated from the MCS and from the IMU gyroscope measurements.

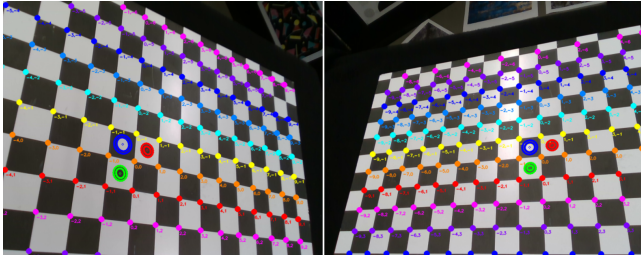


Fig. 6. Corners and fiducial markers detected on the calibration plate.

Parameters	fx	fy	cx	cy	distortion coefficients
factory	605.2	605.1	425.7	246.0	0 0 0 0 0
estimated	599.6	599.2	426.6	246.3	0.1 -0.4 0 0 0.3

TABLE II

INTRINSIC PARAMETERS OF THE CAMERA IN  $[px]$  USED IN OUR DATASET.

maximum at zero offset confirms correct alignment.

### E. Camera calibration

To estimate the hand-eye transformation (i.e., the transformation from the robot flange to the camera projection plane), more than 200 images containing the calibration plate were captured, and the corresponding robot pose for each image was saved. Subsequently, the calibration method presented in [26] was applied. The calibration plate (a chessboard with squares of  $30 \times 30$  mm) was detected by applying a custom detection method (see Fig. 6). The intrinsics of the RealSense D435i camera were refined from the factory calibration ones.

For a more accurate calibration, not only the extrinsic parameters (hand-eye transformation) were estimated, but also the intrinsic parameters. Our experiments have proven that the use of the estimated intrinsic parameters resulted in more accurate extrinsic parameters. The intrinsic parameters of the camera (focal length (fx/fy), principal point (cx/cy) and camera distortion coefficients) are shown in Table II. The extrinsic parameters are shown in the Table III.

To compare the accuracy of the calibration using both factory and estimated intrinsic parameters, the set of calibration images was divided into several batches (10 batches with 20 images in each), and the same calibration process was applied to each batch. The accuracy of the calibration was assessed using the metrics proposed in [27], which include translation error in millimeters ( $Trans. [mm]$ ), rotation error in degrees ( $Rot. [deg.]$ ), and unitless relative transformation error ( $Rel. transf. error [a.u.]$ ).

Table IV shows the mean, standard deviation, and standard error of the calibration metrics. The accuracy of the hand-eye transformation, calculated using the estimated intrinsic parameters, showed more precise results, with reduced re-projection, translation, rotation, and relative transformation errors.

## V. EXPERIMENTS

Used intrinsics	tx	ty	tz	qx	qy	qz	qw
factory	0.5895	32.5419	46.0707	0.0060	0.0041	-0.7035	0.7106
estimated	-0.2852	32.7894	46.1513	0.0063	0.0054	-0.7037	0.7104

TABLE III

EXTRINSIC PARAMETERS (HAND-EYE TRANSFORMATION) OF THE CAMERA, REPRESENTED AS A TRANSLATION VECTOR IN  $[mm]$  AND A UNIT QUATERNION FOR ROTATION.

	Reproj. error [px]	Hand-eye		
		Trans. [mm]	Rot. [deg.]	Rel. transf. err. [a.u.]
Mean	0.36	2.38	0.33	2.90
Std. dev.	0.04	0.41	0.08	0.66
Std. error	0.01	0.13	0.02	0.21
<b>All images (estim. intrinsics)</b>	<b>0.38</b>	<b>2.31</b>	<b>0.31</b>	<b>2.69</b>
All images (factory intrinsics)	0.61	2.37	0.33	2.77

TABLE IV

MEAN, STANDARD DEVIATION AND STANDARD ERROR OF THE CALIBRATION METRICS. THE LAST TWO ROWS SHOW THE RESULTS USING ALL IMAGES WITH THE ESTIMATED AND FACTORY INTRINSIC PARAMETERS.

### A. Metrics

In this work, we report the Root Mean Square Error of the Absolute Trajectory Error (ATE RMSE  $\downarrow$ ) to assess the camera tracking accuracy. To evaluate novel view synthesis, we follow the evaluation protocol presented in [8] and report standard photometric rendering metrics such as Peak Signal-to-Noise Ratio (PSNR  $\uparrow$ ), Structural Similarity Index Measure (SSIM  $\uparrow$ ), and Learned Perceptual Image Patch Similarity (LPIPS  $\downarrow$ ). PSNR captures pixel-level differences, SSIM reflects perceptual similarity in terms of structure, luminance, and contrast [28]. LPIPS evaluates visual fidelity based on deep feature representations [29].

### B. Results

To evaluate the dataset’s suitability for benchmarking methods at the intersection of SLAM and novel view synthesis, we present results from state-of-the-art techniques.

**Novel View Synthesis.** To highlight the usefulness of independent test camera trajectories, we evaluated the performance of two state-of-the-art baselines: Gaussian Splatting [8] and FeatSplat [30] (this last one specifically designed to reduce viewpoint overfitting). In this experiment, *setup-1*, *setup-3*, and *setup-4* were used under natural, warm, and dark lighting conditions. Baselines were initialized with random point-clouds and a black background, using 4 Spherical Harmonics bands for Gaussian Splatting, and 32-dimensional latent vectors and 1 hidden layer of 64 neurons MLP for FeatSplat. They were optimized for a total of 21k iterations, and we report metrics both at 7k and 21k iterations. The baselines were optimized on the respective *train* trajectories of each setup, skipping one every ten frames. We evaluate both with the common approach of using skipped frames from the *train* trajectory [4], [8] (see Table V) and using the independently recorded *test* trajectory of each setup (see Table VI).

	natural			warm			dark		
	PSNR	LPIPS	SSIM	PSNR	LPIPS	SSIM	PSNR	LPIPS	SSIM
gsplat-7k	17.32	0.445	0.694	17.67	0.497	0.609	23.77	0.464	0.678
fsplat-7k	17.40	0.445	0.700	17.75	0.499	0.610	23.43	0.467	0.687
gsplat-21k	18.43	0.411	0.724	18.75	0.468	0.637	24.99	0.443	0.708
<b>fsplat-21k</b>	<b>19.45</b>	<b>0.406</b>	<b>0.743</b>	<b>20.01</b>	<b>0.461</b>	<b>0.656</b>	<b>25.13</b>	<b>0.444</b>	<b>0.714</b>

TABLE V

CLASSIC EVALUATION OF GAUSSIAN SPLATTING (GSPLAT) AND FEATSPLAT (FSPLAT) REPORTING PSNR[↑], LPIPS[↓], AND SSIM[↑].

	natural			warm			dark		
	PSNR	LPIPS	SSIM	PSNR	LPIPS	SSIM	PSNR	LPIPS	SSIM
gsplat-7k	14.53	0.493	0.608	<b>15.45</b>	0.543	0.527	21.82	0.499	<b>0.596</b>
fsplat-7k	<b>14.73</b>	0.488	<b>0.623</b>	15.42	0.541	<b>0.540</b>	21.73	0.498	0.630
gsplat-21k	14.42	<b>0.478</b>	0.606	15.35	<b>0.531</b>	0.524	21.53	0.492	0.600
fsplat-21k	14.71	<b>0.478</b>	0.614	15.29	0.532	0.535	<b>21.91</b>	<b>0.490</b>	0.627

TABLE VI

EVALUATION ON INDEPENDENT TEST TRAJECTORY OF GAUSSIAN SPLATTING (GSPLAT) AND FEATSPLAT (FSPLAT) REPORTING PSNR[↑], LPIPS[↓], AND SSIM[↑].

The common evaluation indicates an improvement in rendering performance, for both baselines, through the complete optimization process (see Table V). Both baselines achieve their best performance under *dark* lighting conditions, which is probably due to using black as initial background color. Nevertheless, the test trajectory at **SLAM&Render** reveals that both baselines overfit to the training trajectory. Note how the rendering quality does not improve beyond the 7k iteration and even slightly declines in Table VI. Qualitative analysis in Fig. 7 also showcases the contrast between the high quality rendering of validation viewpoints and the artifacts generated in test viewpoints. This result validates the need for datasets with independent trajectories to evaluate novel view synthesis methods and shows that the classic approach of sampling evaluation frames from the training



Fig. 7. Comparison of Novel View Synthesis for validation and test viewpoints. Despite both models perform well when evaluated on validation viewpoints of the training trajectory, the independent test trajectory reveals overfitting.

Setup	Ill.	Traj.	MonoGS	Kinematics	MonoGS (Kinem. seed)
setup-1	natural	train	3.3	0.5	2.0
	natural	test	3.9	0.4	2.1
	cold	test	2.4	0.3	2.2
	warm	test	2.1	0.3	1.4
	dark	test	3.1	0.4	1.9
setup-3	natural	train	2.6	0.5	1.1
	natural	test	3.7	0.4	1.7
	dark	train	0.6	0.5	0.6
	dark	test	3.8	0.3	1.6
setup-4	natural	train	0.9	0.5	0.7
	cold	train	2.4	0.5	1.0
	warm	train	1.6	0.5	0.8
	dark	train	1.0	0.5	0.9

TABLE VII

ATE RMSE [↓ cm] ON DIFFERENT SEQUENCES RUNNING THREE ALGORITHM CONFIGURATIONS: MONOGS, KINEMATICS AND MONOGS WITH KINEMATIC DATA AS SEED

trajectory does not inform about trajectory overfitting.

**Camera tracking.** To illustrate the advantage on using kinematic data, three approaches based on Gaussian Splatting SLAM [9] (MonoGS) were evaluated. In the first experiment, we used the default configuration for MonoGS. In the second experiment we incorporated the robot kinematic data directly as the camera motion. This approach is referred to as the *Kinematics* experiment. In the third experiment, robot kinematics were incorporated as an initial seed for camera pose estimation within MonoGS. This is referred to as *Kinem. seed* experiment. Following the evaluation conducted by the authors of MonoGS in [9], the ATE RMSE for keyframes is reported in Table VII. For this experiment, *setup-1*, *setup-3*, and *setup-4* were used under different light conditions while performing *train* and *test* trajectories. In all cases, it is evident that incorporating kinematic data improves camera tracking performance. However, the results also show that the naive approach of using robot kinematics as the initial seed of MonoGS decreases its accuracy. This result motivates the use of our **SLAM&Render** dataset for research on multimodal fusion within NeRF and Gaussian Splatting SLAM. Fig. 8 illustrates the camera tracking results for *setup-4* under cold lighting condition. The trajectory using MonoGS is shown in Fig. 8a, while Fig. 8b shows the result using kinematic data as initial seed. Incorporating kinematic data allows drift

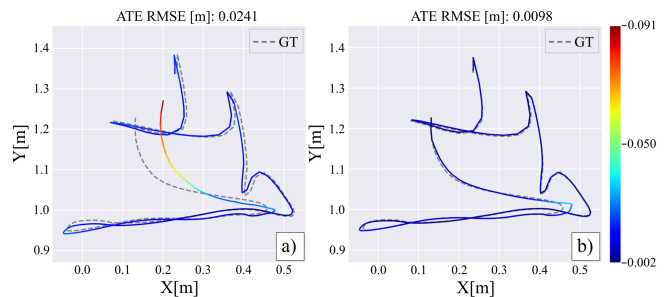


Fig. 8. Camera tracking result for *setup-4* under cold light using a) MonoGS and b) MonoGS with kinematic data as initial seed. Dashed line represent the ground-truth while colored line represent the camera trajectory. Incorporating kinematic data allows drift correction in camera tracking.

correction in camera tracking.

## VI. CONCLUSIONS

In this work we introduced **SLAM&Render**, a dataset for benchmarking methods that combine SLAM and novel view rendering. Our data includes 40 sequences of synchronized RGB and depth images, IMU readings, robot kinematic data, intrinsic and extrinsic camera parameters, and ground-truth pose data across diverse scenes and conditions. **SLAM&Render** addresses research challenges such as generalization across trajectories and robustness to scene and illumination changes. By releasing robot kinematic data, it also enables the assessment of novel SLAM strategies when applied to robot manipulators. It aims to drive future research in learning-based and hybrid methods requiring accurate localization and multi-sensor data fusion, ultimately enhancing the deployment of systems that combine perception, mapping, and rendering.

## VII. ACKNOWLEDGMENTS

The authors would like to thank the Technology & Innovation Center of KUKA Deutschland GmbH (Augsburg, Germany) for their support and resources provided during the course of this research.

## REFERENCES

- [1] C. Campos, R. Elvira, J. J. G. Rodríguez, J. M. Montiel, and J. D. Tardós, “Orb-slam3: An accurate open-source library for visual, visual-inertial, and multimap slam,” *IEEE transactions on robotics*, vol. 37, no. 6, pp. 1874–1890, 2021.
- [2] C. Cadena, L. Carlone, H. Carrillo, Y. Latif, D. Scaramuzza, J. Neira, I. Reid, and J. J. Leonard, “Past, present, and future of simultaneous localization and mapping: Toward the robust-perception age,” *IEEE Transactions on robotics*, vol. 32, no. 6, pp. 1309–1332, 2016.
- [3] J. L. Schonberger and J.-M. Frahm, “Structure-from-motion revisited,” in *Proceedings of the IEEE conference on computer vision and pattern recognition*, 2016, pp. 4104–4113.
- [4] B. Mildenhall, P. P. Srinivasan, M. Tancik, J. T. Barron, R. Ramamoorthi, and R. Ng, “Nerf: Representing scenes as neural radiance fields for view synthesis,” *Communications of the ACM*, vol. 65, no. 1, pp. 99–106, 2021.
- [5] E. Sucar, S. Liu, J. Ortiz, and A. J. Davison, “imap: Implicit mapping and positioning in real-time,” in *Proceedings of the IEEE/CVF international conference on computer vision*, 2021, pp. 6229–6238.
- [6] Z. Zhu, S. Peng, V. Larsson, W. Xu, H. Bao, Z. Cui, M. R. Oswald, and M. Pollefeys, “Nice-slam: Neural implicit scalable encoding for slam,” in *Proceedings of the IEEE/CVF conference on computer vision and pattern recognition*, 2022, pp. 12 786–12 796.
- [7] J. Deng, Q. Wu, X. Chen, S. Xia, Z. Sun, G. Liu, W. Yu, and L. Pei, “Nerf-loam: Neural implicit representation for large-scale incremental lidar odometry and mapping,” in *Proceedings of the IEEE/CVF International Conference on Computer Vision*, 2023, pp. 8218–8227.
- [8] B. Kerbl, G. Kopanas, T. Leimkühler, and G. Drettakis, “3d gaussian splatting for real-time radiance field rendering,” *ACM Trans. Graph.*, vol. 42, no. 4, pp. 139–1, 2023.
- [9] H. Matsuki, R. Murai, P. H. Kelly, and A. J. Davison, “Gaussian splatting slam,” in *Proceedings of the IEEE/CVF Conference on Computer Vision and Pattern Recognition*, 2024, pp. 18 039–18 048.
- [10] N. Keetha, J. Karhade, K. M. Jatavallabhula, G. Yang, S. Scherer, D. Ramanan, and J. Luiten, “Splatam: Splat track & map 3d gaussians for dense rgb-d slam,” in *Proceedings of the IEEE/CVF Conference on Computer Vision and Pattern Recognition*, 2024, pp. 21 357–21 366.
- [11] V. Yugay, Y. Li, T. Gevers, and M. Oswald, “Gaussian-slam: Photo-realistic dense slam with gaussian splatting,” *arXiv preprint arXiv:2312.10070*, 2023.
- [12] M. Li, S. Liu, H. Zhou, G. Zhu, N. Cheng, T. Deng, and H. Wang, “Sgs-slam: Semantic gaussian splatting for neural dense slam,” in *European Conference on Computer Vision*. Springer, 2024, pp. 163–179.
- [13] F. Tosi, Y. Zhang, Z. Gong, E. Sandström, S. Mattoccia, M. R. Oswald, and M. Poggi, “How nerfs and 3d gaussian splatting are reshaping slam: a survey,” *arXiv preprint arXiv:2402.13255*, vol. 4, p. 1, 2024.
- [14] R. Jensen, A. Dahl, G. Vogiatzis, E. Tola, and H. Aanæs, “Large scale multi-view stereopsis evaluation,” in *Proceedings of the IEEE conference on computer vision and pattern recognition*, 2014, pp. 406–413.
- [15] Y. Gao, S. S. Vedula, C. E. Reiley, N. Ahmadi, B. Varadarajan, H. C. Lin, L. Tao, L. Zappella, B. Béjar, D. D. Yuh, *et al.*, “Jhu-isi gesture and skill assessment working set (jigsaws): A surgical activity dataset for human motion modeling,” in *MICCAI workshop: M2cai*, vol. 3, no. 2014, 2014, p. 3.
- [16] B. Calli, A. Singh, A. Walsman, S. Srinivasa, P. Abbeel, and A. M. Dollar, “The ycb object and model set: Towards common benchmarks for manipulation research,” in *2015 international conference on advanced robotics (ICAR)*. IEEE, 2015, pp. 510–517.
- [17] M. Burri, J. Nikolic, P. Gohl, T. Schneider, J. Rehder, S. Omari, M. W. Achtelik, and R. Siegwart, “The euroc micro aerial vehicle datasets,” *The International Journal of Robotics Research*, vol. 35, no. 10, pp. 1157–1163, 2016.
- [18] A. Knapitsch, J. Park, Q.-Y. Zhou, and V. Koltun, “Tanks and temples: Benchmarking large-scale scene reconstruction,” *ACM Transactions on Graphics*, vol. 36, no. 4, 2017.
- [19] D. Schubert, T. Goll, N. Demmel, V. Usenko, J. Stückler, and D. Cremers, “The tum vi benchmark for evaluating visual-inertial odometry,” in *2018 IEEE/RSJ International Conference on Intelligent Robots and Systems (IROS)*. IEEE, 2018, pp. 1680–1687.
- [20] X. Shi, D. Li, P. Zhao, Q. Tian, Y. Tian, Q. Long, C. Zhu, J. Song, F. Qiao, L. Song, *et al.*, “Are we ready for service robots? the openloris-scene datasets for lifelong slam,” in *2020 IEEE international conference on robotics and automation (ICRA)*. IEEE, 2020, pp. 3139–3145.
- [21] J. Straub, T. Whelan, L. Ma, Y. Chen, E. Wijmans, S. Green, J. J. Engel, R. Mur-Artal, C. Ren, S. Verma, *et al.*, “The replica dataset: A digital replica of indoor spaces,” *arXiv preprint arXiv:1906.05797*, 2019.
- [22] J. T. Barron, B. Mildenhall, D. Verbin, P. P. Srinivasan, and P. Hedman, “Mip-nerf 360: Unbounded anti-aliased neural radiance fields,” *CVPR*, 2022.
- [23] C. Yeshwanth, Y.-C. Liu, M. Nießner, and A. Dai, “Scannet++: A high-fidelity dataset of 3d indoor scenes,” in *Proceedings of the IEEE/CVF International Conference on Computer Vision*, 2023, pp. 12–22.
- [24] J. Sturm, N. Engelhard, F. Endres, W. Burgard, and D. Cremers, “A benchmark for the evaluation of rgb-d slam systems,” in *2012 IEEE/RSJ International Conference on Intelligent Robots and Systems*, 2012, pp. 573–580.
- [25] A. Bonarini, W. Burgard, G. Fontana, M. Matteucci, D. G. Sorrenti, J. D. Tardos, *et al.*, “Rawseeds: Robotics advancement through web-publishing of sensorial and elaborated extensive data sets,” in *In proceedings of IROS*, vol. 6, 2006, p. 93.
- [26] Y. Shiu and S. Ahmad, “Calibration of wrist-mounted robotic sensors by solving homogeneous transform equations of the form  $ax=xb$ ,” *IEEE Transactions on Robotics and Automation*, vol. 5, no. 1, pp. 16–29, 1989.
- [27] I. Enebus, B. K. S. M. K. Ibrahim, M. Foo, R. S. Matharu, and H. Ahmed, “Accuracy evaluation of hand-eye calibration techniques for vision-guided robots,” *PLOS ONE*, vol. 17, no. 10, pp. 1–26, 10 2022.
- [28] Z. Wang, A. Bovik, H. Sheikh, and E. Simoncelli, “Image quality assessment: from error visibility to structural similarity,” *IEEE Transactions on Image Processing*, vol. 13, no. 4, pp. 600–612, 2004.
- [29] R. Zhang, P. Isola, A. A. Efros, E. Shechtman, and O. Wang, “The unreasonable effectiveness of deep features as a perceptual metric,” in *Proceedings of the IEEE Conference on Computer Vision and Pattern Recognition (CVPR)*, June 2018.
- [30] T. B. Martins and J. Civera, “Feature splatting for better novel view synthesis with low overlap,” in *35th British Machine Vision Conference 2024, BMVC 2024, Glasgow, UK, November 25-28, 2024*. BMVA, 2024.